NANO LETTERS

pubs.acs.org/NanoLett

Letter

Anisotropic Thermal Conductivity of Crystalline Layered $SnSe_2$

Peng Xiao,[⊥] Emigdio Chavez-Angel,[⊥] Stefanos Chaitoglou, Marianna Sledzinska, Athanasios Dimoulas, Clivia M. Sotomayor Torres, and Alexandros El Sachat*

Cite This: *Nano Lett.* 2021, 21, 9172−9179

Read Online

ACCESS | Metrics & More | Article Recommendations | Supporting Information

ABSTRACT: The degree of thermal anisotropy affects critically key device-relevant properties of layered two-dimensional materials. Here, we systematically study the in-plane and cross-plane thermal conductivity of crystalline $SnSe_2$ films of varying thickness (16−190 nm) and uncover a thickness-independent thermal conductivity anisotropy ratio of about ∼8.4. Experimental data obtained using Raman thermometry and frequency domain thermoreflectance showed that the in-plane and cross-plane thermal conductivities monotonically decrease by a factor of 2.5 with decreasing film thickness compared to the bulk values. Moreover, we find that the temperature-dependence of the in-plane component gradually decreases as the film becomes thinner, and in the range from 300 to 473 K it drops by more than a factor of 2. Using the mean free path reconstruction method, we found that phonons with MFP ranging from ∼1 to 53 and from 1 to 30 nm contribute to 50% of the total in-plane and cross-plane thermal conductivity, respectively.

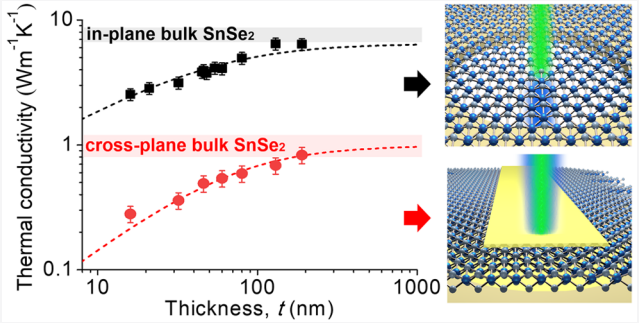

KEYWORDS: *Phonon transport, mean free path, $SnSe_2$, thermal conductivity anisotropy, frequency-domain thermoreflectance, Raman thermometry*

Understanding the propagation of heat in two-dimensional (2D) materials is of paramount importance to establish its potential in, for example, energy harvesting in thermal management in future nanoelectronic devices. $SnSe_2$ is a promising 2D material with desirable properties such as relatively high electron mobility of ∼85 $cm^2\ V^{-1}\ s^{-1}$ at room temperature,[1] high bulk electron affinity of 5.2 eV,[2] and low thermal conductivity according to recent first principle calculations.[3−6] It has already shown excellent performance in field-effect transistors (FETs),[7−9] phase-change memory,[10] and optoelectronic devices,[11] and recently it has been suggested that it is an ideal layered material for thermoelectric applications.[3,5,12] In particular, recent calculations have shown that at 800 K the thermoelectric figure of merit in *a* and *c* directions can reach values as high as 2.95 and 0.68, respectively.[12]

While extensive electrical and optical characterization of $SnSe_2$ is available,[13−17] experimental studies on the intrinsic thermal properties of $SnSe_2$ are few and far between.[18,19] To date, the thickness-dependence of the in-plane thermal conductivity (k_r) has been investigated only in a few samples grown by chemical vapor deposition in a narrow range of thickness using the traditional optothermal Raman technique.[18] Moreover, there are no reports on measurements of the cross-plane thermal conductivity (k_z) in $SnSe_2$; thus its anisotropic thermal properties have so far not been experimentally investigated.

In this work, we study the in-plane and cross-plane thermal conductivity of crystalline $SnSe_2$ films with thickness between 16 and 190 nm using two different thermal characterization techniques, namely, Raman thermometry and frequency domain thermoreflectance (FDTR). We focus on unraveling the influence of film thickness on k_r and k_z in suspended and supported $SnSe_2$, respectively, from which we obtain the thermal conductivity anisotropy ratio. In addition, we study the effect of film thickness on the temperature-dependent k_r of suspended $SnSe_2$ films. Finally, using the mean free path reconstruction method,[20−22] we extract the in-plane and cross-plane phonon mean free path (MFP) distribution, showing that the main contribution to the thermal transport is made by phonons with MFPs of tens to hundreds of nanometers.

The $SnSe_2$ films were mechanically exfoliated from single crystals (purchased from HQ Graphene) by the assistance of a viscoelastic stamp (GelPak)[23] onto gold-coated silicon nitride substrates with 20 and 30 μm holes. Schematics of the $SnSe_2$ crystal structure are shown in Figure 1a. The crystal and

Received: August 5, 2021
Revised: October 12, 2021
Published: October 28, 2021

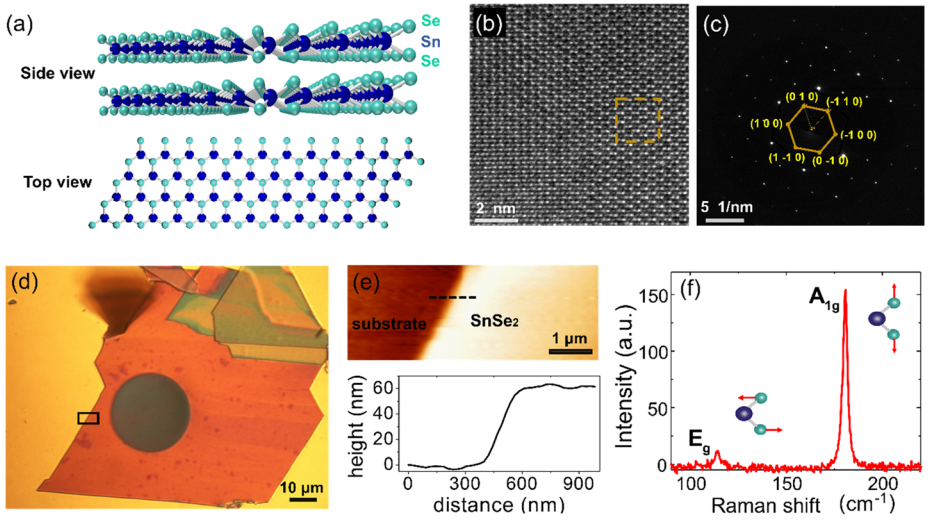

Figure 1. (a) Side and top views of the $SnSe_2$ crystal structure. Each $SnSe_2$ layer consists of three atomic sublayers, in which Sn atoms (blue spheres) are sandwiched between Se atoms (green spheres). (b) HR-STEM image of a 30 nm thick exfoliated suspended $SnSe_2$ film and (c) Fourier transform of the squared region depicted in (b), from which we extract the a and b lattice constants, $a = b = 0.387$ nm. (d) Representative optical image of a 60 nm thick $SnSe_2$ film. The diameter of the suspended circular area is 30 μm. (e) AFM image of the region outlined by the rectangle box in (d) and the corresponding measured height profile along the dashed black line in the topography image. (f) Raman spectrum of a 60 nm thick $SnSe_2$ film using an excitation wavelength of 532 nm and a 50× objective. In the inset to (f), red arrows indicate the direction of the movement of Sn and Se atoms.

morphological characterization of the samples was studied by high-resolution scanning transmission electron microscopy (HR-STEM), atomic force microscopy (AFM), and Raman spectroscopy measurements. Figure 1b and Figure 1c display the planar HR-STEM and the corresponding electron diffraction image, respectively, of a 30 nm thick $SnSe_2$ suspended film. The high-magnification HR-STEM image (Figure 1b) depicts a honeycomb arrangement of atoms, indicating the single-crystalline structure. The simulated FFT pattern (yellow spots in the inset of Figure 1c) displays hexagonal symmetrical patterns, indicating the hexagonal lattice structure of the $SnSe_2$. From the simulations, we extracted the in-plane lattice constants $a = b = 0.387$ nm, in very good agreement with the literature.[24,25] Figure 1d displays a representative optical image of a 60 nm thick suspended exfoliated $SnSe_2$ film. The AFM topography image of the interface between the substrate and the exfoliated film together with the corresponding height profile is shown in Figure 1e. All the thicknesses of the $SnSe_2$ films were measured in tapping mode by AFM (see Supporting Information). The chemical structure of $SnSe_2$ was confirmed by Raman spectroscopy as shown in Figure 1f. The crystalline $SnSe_2$ exhibits two Raman active vibrational modes at 113 cm^{-1} (E_g) and 180 cm^{-1} (A_{1g}), in agreement with previous reports.[19,26]

The k_r of suspended $SnSe_2$ films at room temperature was measured by using our steady-state two-laser Raman thermometry technique.[27−29] In this approach, a hot spot is produced by a heating laser with wavelength $\lambda_1 = 405$ nm fixed in the center of a suspended film, while a second laser with $\lambda_2 = 532$ nm measures the temperature distribution based on a calibration of its Raman spectra with temperature (see Figure 2a). In these measurements, we monitored the temperature through the frequency of the longitudinal (LO) optical phonons of $SnSe_2$ at ∼180 cm^{-1}. Both lasers were focused using a 50× NA = 0.55 objective. The main advantage of this approach, with respect to the conventional optothermal Raman technique, is that no assumption has to be made to obtain the thermal conductivity since it yields directly maps of the thermal field, both connected through the Fourier's law, $Q/A = -k_r T$, where Q is the heat flux, A is the area of the heat flux, and T is the temperature.

We point out that for the in-plane thermal conductivity measurements it is important to ensure that the phonons with large MFP are not affected by the lateral dimensions. For the case of graphene, the in-plane MFP distribution is very broad (200 nm to 10 μm)[30] and the impact of the lateral dimensions on the in-plane thermal conductivity has been detected experimentally.[31] However, in our experiments the lateral size effect should not affect the measured thermal conductivity considering that $SnSe_2$ has MFP distribution (1−1000 nm)[6,12] much smaller than the size of the suspended films and the heat sink is located 10 or 15 μm away from the heating area. In the two-dimensional case, where no temperature gradients are present in the third dimension and for temperature ranges that exhibit a purely diffusive heat transport regime, the radial symmetry of the temperature distribution upon a Gaussian thermal excitation allows reduction of Fourier's law to its one-dimensional form depending only on the radial coordinate r and the area $A = 2\pi rt$, where t is the thickness of the suspended film. Thus, the Fourier law gives a simple expression for the thermal conductivity as follows:

$$k_r(T) = \frac{-P_0}{2\pi t \xi(r)} \tag{1}$$

where P_0 is the absorbed power by the film and $\xi(r) = dT/(d \ln r)$. In the case of a temperature-independent thermal conductivity in the temperature range under study, the thermal field decays as $T(r) \propto \ln r$ in the diffusive limit and k_r is directly obtained from eq 1 after extracting $\xi(r)$ from the slope of a linear fit to the logarithmic temperature profile and by measuring P_0 and t. We note that this procedure is valid for a data range starting at a distance of a few micrometers from the central point $r = 0$, where diffusive transport dominates.

https://doi.org/10.1021/acs.nanolett.1c03018
Nano Lett. 2021, 21, 9172−9179

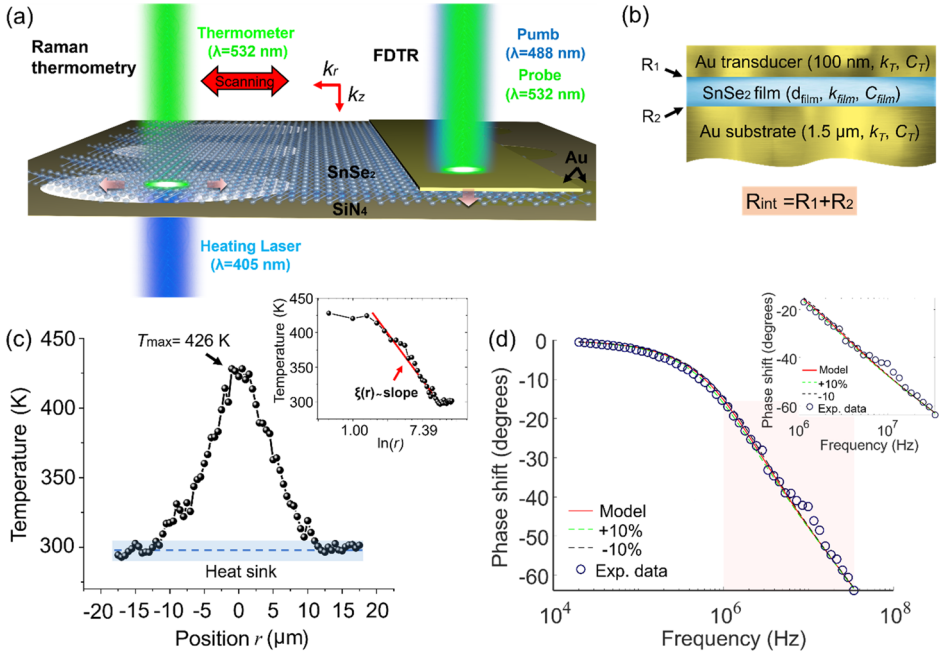

Figure 2. Schematics of (a) the two-laser Raman thermometry and FDTR experimental configurations and (b) the multilayer structure (Au/$SnSe_2$/Au) with the two interface thermal resistances R_1 and R_2. (c) Representative temperature profile of a 16 nm thick suspended $SnSe_2$ film with a maximum temperature rise at the heating spot at the center of the membrane of T_{max} = 426 K. The inset shows the linear fit of the temperature profile in logarithmic scale from which we extract the logarithmic derivate $\xi(r) \sim dT/(d \ln r)$. (d) Typical FDTR data measured in a 130 nm thick supported $SnSe_2$ film (blue circles) and the corresponding best model fit (red curve) in the whole frequency range. The light red area indicates the fitting frequency range used to extract R_1 and R_2, and the inset to (d) shows the fitting of the experimental data in this range.

A representative temperature profile of the 16 nm thick suspended $SnSe_2$ film is shown in Figure 2c. The temperature accuracy was ±2 K with a spatial resolution better than 600 nm (given by λ_2). The inset to Figure 2c shows the linear fit of the measured temperature profile in logarithmic scale. For each sample we measured a line scan $T(r)$ fulfilling the condition that the maximum temperature is that at the heating laser spot at $r = 0$. The range r was chosen to observe as full relaxation as possible of the temperature field to the heat sink temperature, T_{sink} = 300 K. However, preliminary measurements indicated that this depends on the thermal conductivity of each sample. Then, to improve the efficiency of the heat sink at the boundaries, we deposited 100 nm Au layer on the SiN_4 substrates and later the films were deposited. The measured k_r values are plotted in Figure 3a. All the measurements were conducted in vacuum at 10^{-3} mbar to avoid heat conduction through the air.[29] The experimental data of the thickness-dependent absorbance at room temperature are shown in Figure S12 in the Supporting Information.

To measure k_z of the $SnSe_2$ films, we performed pump-and-probe experiments using the FDTR technique.[32,33] The experimental setup is based on two lasers operating at 488 nm (pump) and 532 nm (probe). The modulated pump beam is focused on the $SnSe_2$ samples using a 50× objective, creating a periodic heat flux with a Gaussian spatial distribution on the sample surface (see Figure 2a). The reflected low power probe beam is aligned with the pump beam and focused with the pump spot to monitor temperature variation through changes in optical reflectivity of the surface. We used a lock-in amplifier (Zurich Instruments HF2LI) to record the amplitude and phase response of the reflected probe beam to the thermal wave. The pump signal was used as reference while the phase lag between the pump and probe beam as the observable quantity.

Prior to the FDTR measurements 100 nm and 1.5 μm thick Au layers are deposited on the top and bottom of the suspended films, respectively. The top Au layers were used as transducers, while the thick bottom Au layers become the substrates. Therefore, our multilayer system consists of Au/$SnSe_2$/Au stacks (see Figure 2b). For each $SnSe_2$ film we obtained frequency-domain measurements and extracted the k_z following a multilayer three-dimensional heat diffusion model.[34] This model requires material parameters such as the volumetric heat capacity (C), thickness, interface thermal resistance, and k_z. The thermal conductivity and volumetric heat capacity of Au as well as the volumetric specific heat of $SnSe_2$ were taken from the literature.[32,35] The thickness of the Au transducer layer was measured by AFM (see Figure S1d,e of the Supporting Information). Thus, the remaining parameters are the k_z of $SnSe_2$, the thermal resistance of the top layer Au/$SnSe_2$ interface (R_1), and the thermal resistance of the $SnSe_2$/Au (substrate) interface (R_2). To quantify the sensitivity of the measured phase signal to different parameters in the case of Au/$SnSe_2$/Au stacks, a sensitivity analysis is carried out in a similar manner to that of Schmidt et al.[34] In Figure S2 of the Supporting Information we show the calculated phase sensitivity ($-V_{in}/V_{out}$) to multiple parameters (k_z, C, anisotropy, R_1, and R_2) as a function of thickness and modulation frequency. From this analysis we found that the sensitivity of the recorded phase signal strongly depends on the modulation frequency; thus it is possible to extract different thermal properties directly from the model fit of the experimental data in a specific frequency range. In Figure S3 we also show the phase sensitivity as a function of the modulation frequency for the case of a 16 nm thick $SnSe_2$ film.

https://doi.org/10.1021/acs.nanolett.1c03018
Nano Lett. 2021, 21, 9172−9179

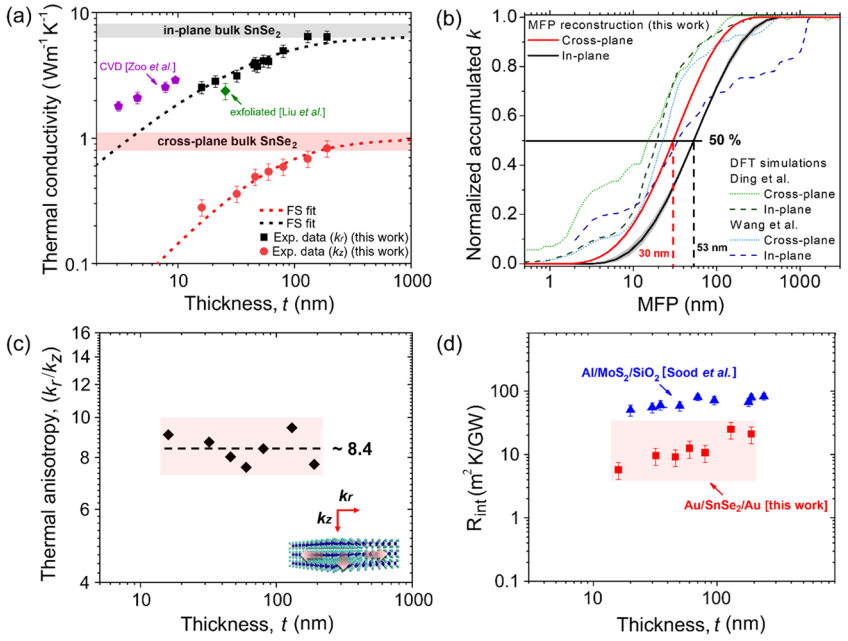

Figure 3. (a) In-plane (black squares) and cross-plane (red circles) thermal conductivities of exfoliated $SnSe_2$ films with thickness between 16 and 190 nm measured with 2LRT and FDTR. The in-plane[32,33] and cross-plane[19,34] Fuchs−Sondheimer (FS) fits to the experimental data are indicated with black and red dashed lines, respectively. The light gray and red areas display the calculated in-plane and cross-plane bulk thermal conductivities taken from the literature.[6,12] The errors in k_z were estimated by the standard deviation of several measurements, including the numerical errors from the fits. The errors in k_r were obtained from the error propagation of each parameter of eq 1. (b) Normalized accumulated thermal conductivity as a function of the phonon MFP (red and black solid curves). In dashed curves we plot the phonon MFP distribution in bulk $SnSe_2$ calculated by Wang et al.[6] and Ding et al.[12] (c) Thermal conductivity anisotropy (k_r/k_z) as a function of $SnSe_2$ film thickness. (d) Total interface thermal resistance, $R_{int} = R_1 + R_2$ (red squares), plotted versus film thickness extracted from the FDTR measurements. Previous total interface thermal resistance calculations on $Al/MoS_2/SiO_2$ (blue triangles) where similar interfacial contributions from bottom (2D material/substrate) and top (metal/2D material) interfaces were taken into account.

In particular, to extract the k_z of each film from a single FDTR measurement, we followed a fitting approach similar to that used in previous works[34,36] and supported by our sensitivity analysis. First, we extract k_z by fitting the experimental data in a low frequency range (20 kHz to 1 MHz), where the phase signal sensitivity to R_1, R_2, and heat capacity of the films is negligible. Then, we fix k_z and fit the experimental data in a high frequency range (1−40 MHz) to estimate simultaneously R_1 and R_2. For the first estimate to determine the value of the free parameters (k_z, R_1, and R_2), we used previous reported values of similar materials.[37−39] A typical example of the recorded phase signal and corresponding best model fit for a 130 nm thick $SnSe_2$ film is shown in Figure 2d. The inset to Figure 2d shows the fitting of our experimental data in the high frequency range.

Figure 3a displays the measured k_r and k_z values for all the $SnSe_2$ films with thicknesses between 16 and 190 nm. We observe that both k_r and k_z monotonically increase with increasing thickness and reach the calculated bulk in-plane and cross-plane thermal conductivity values, respectively.[6,12] In particular, the k_r values range from 6.45 ± 0.71 W m^{-1} K^{-1} for the thickest film (t = 190 nm) down to 2.54 ± 0.31 W m^{-1} K^{-1} for the thinnest film (t = 16 nm), which corresponds to about a 2.5-fold reduction. A similar decrease was observed in the k_z, with the values dropping from 0.83 ± 0.12 W m^{-1} K^{-1} in the thickest $SnSe_2$ film down to 0.28 ± 0.05 in the thinnest film. We note that the linear k_z increase with increasing thickness might indicate quasi-ballistic phonon propagation, similar to previous experiments in MoS_2;[40] however, more calculations are necessary to conclude. In the same graph we plot previously reported in-plane thermal conductivity data in CVD and exfoliated $SnSe_2$ by Zou et al.[18] and Liu et al.,[19] respectively, which are in good agreement with our measurements.

The origin of the k_r and k_z decreasing with decreasing film thickness can be understood considering phonon diffuse (incoherent) boundary scattering at the surface of the films as the main scattering mechanism. In particular, at room temperature the only characteristic dimension that dominates phonon scattering is the thickness of the $SnSe_2$ films. Thus, t is the dimension that sets a cutoff to the phonon-MFP due to diffuse boundary scattering, i.e., phonons with MFP > t will not fully propagate, thus reducing their contribution to k_r and k_z. Moreover, the similar rate of increase of k_r and k_z with increasing film thickness observed in Figure 3a suggests that phonons with MFP commensurate with the sample thickness contribute to the thermal conductivity.

To gain a further insight on how phonons contribute to the thermal conductivity, we use the MFP reconstruction model to extract the cross-plane and in-plane phonon MFP distribution (see details in Supporting Information). A detailed description of this model can be found elsewhere.[20−22,41−43] Figure 3b displays the normalized accumulated thermal conductivity as a function of the phonon MFP. It is seen that the MFP distribution shifts to longer values for in-plane transport compared to the cross-plane. In particular, we found that phonons with MFP ranging from 1 to 53 nm and from 1 to 30 nm contribute to 50% of the k_r and k_z, respectively. Similar observations were also predicted by Wang et al.[6] and Ding et al.[12] in $SnSe_2$ bulk using DFT calculations, while the same

https://doi.org/10.1021/acs.nanolett.1c03018
Nano Lett. 2021, 21, 9172−9179

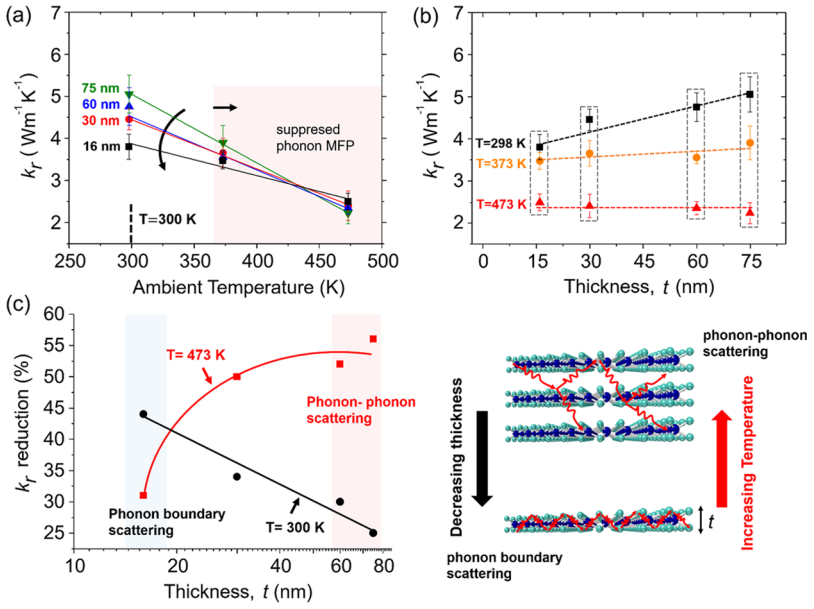

Figure 4. Influence of ambient temperature and thickness on the in-plane thermal conductivity of $SnSe_2$ films. (a) Temperature and (b) thickness dependence of k_r for a series of suspended crystalline $SnSe_2$ films with thickness between 16 and 75 nm, from 300 to 473 K. The *y*-axis in (a) and (b) shows the extracted thermal conductivities using single laser Raman thermometry measurements and FEM simulations (see details in Supporting Information). The *x*-axis in (a) and the temperatures indicated in (b) correspond to the ambient temperatures inside the cryostat. The rectangular dashed regions depicted in (b) show the gradual weaker temperature dependence of k_r with decreasing thickness (c) The percentage of the k_r decrease at 300 K with respect to the bulk $SnSe_2$ value (black full circles) and the percentage of decrease of k_r at 473 K with respect to the k_r at 300 K (red full squares). The black line and red curve are a guide for the eye. The right image in (c) depicts the dominant scattering mechanisms with decreasing thickness and increasing temperature.

methodology was used by Zhang et al.[21] to estimate the MFP distribution in graphite. From the experimental k_r and k_z values, we directly obtain the anisotropy ratio k_r/k_z for each film thickness, as is shown in Figure 3c. The average value of k_r/k_z is 8.4 ± 1, which is in close agreement with theoretical calculations that showed a thermal anisotropy ratio of 7.1 in the $SnSe_2$ bulk sample.[6]

Our result is also in agreement with a recent experimental study that showed a similar thickness-independent thermal anisotropy ratio (∼10) in InSe thin films using time-domain thermoreflectance measurements.[44] Moreover, in Figure 3d we plot the calculated total interface thermal resistance, $R_{tot} = R_1 + R_2$, as a function of film thickness and compare our values with those of supported MoS_2 films also extracted using time-domain thermoreflectance measurements.[40] The observed variation of R_{int} can be attributed to the sample processing (exfoliation and transfer conditions, storage before gold evaporation, etc.), which could result in different interfacial energy coupling. However, we cannot exclude the possibility that R_{int} is increased due to reduced mechanical coupling of the films to the underlying Au resulting from a potential increase in sample stiffness or changes in the vibrational spectra as the thickness is increasing. Similar thickness-dependent R_{int} has been found in MoS_2, InSe, and graphene stacks.[40,44,45]

To examine the dependence of k_r of suspended $SnSe_2$ films on temperature, we conducted single-laser Raman thermometry measurements at different ambient conditions. The k_r of the $SnSe_2$ films was extracted by measuring the absorbed power and the temperature rise of the films at the laser spot at different ambient temperatures (298, 373, and 473 K) and solving the 2D heat equation, as described in detail in our previous work.[46] The temperature of each suspended membrane at the laser spot as a function of the absorbed power at different ambient temperatures is shown in Figure S7 in the Supporting Information. The temperature coefficient (−0.0107 ± 0.0015 K/(cm^{-1})) was determined in advance through a calibration procedure (see Figure S6 in Supporting Information). A deeper analysis of the power measurements and the FEM simulations is given in the Supporting Information (see Figures S9 and S10).

Figure 4a shows the measured k_r of four suspended $SnSe_2$ films with t = 16, 25, 60, and 75 nm as a function of ambient temperature. We observe a systematic decrease of the k_r with increasing temperature for all the $SnSe_2$ films and a maximum reduction of ∼56% at 473 K for the thickest $SnSe_2$ film compared to the room temperature value. This trend originates in the temperature dependence of the phonon MFP, since with increasing temperature the thermal phonon MFP becomes shorter as higher energy phonon states are populated.[47] Therefore, the decrease of k_r with increasing temperature can be attributed to the phonon MFP suppression due to phonon−phonon scattering processes, as has previously been reported in thin film semiconductors at high temperatures.[29,48,49] Furthermore, by plotting k_r as a function of thickness at different ambient temperatures (Figure 4b), we observe that the dependence of k_r with temperature becomes weaker for thinner samples. In other words, as the temperature increases, k_r becomes less sensitive to the sample thickness since these phonons responsible for most of the heat transport have a MFP shorter than the film thickness. The weaker temperature dependence in thinner films seems to be reasonable given that phonon boundary scattering becomes dominant.

In Figure 4c we show the importance of different scattering mechanism by plotting the percentage of the k_r decrease at 300 K with respect to the bulk $SnSe_2$ value (black points) and the percentage of the k_r decrease at 473 K with respect to the k_r at

https://doi.org/10.1021/acs.nanolett.1c03018
Nano Lett. 2021, 21, 9172−9179

300 K (red points). The nearly linear behavior of the black data points is analogous to the observed linear thickness-dependent behavior of k_r (see Figure 3a) and suggests that at room-temperature phonon boundary scattering becomes dominant with decreasing thickness. On the other hand, from the red data points we observe the dominant role of phonon−phonon scattering processes at high temperatures as the film thickness increases. The competing role of the two different scattering mechanisms is illustrated in Figure 4c (right image).

We point out that phonons with MFP longer than the film thickness still contribute to the thermal conductivity provided that phonons wavevector directions are close to the direction of the temperature gradient. However, at high temperatures, the wavelength of phonons dominating the heat transport becomes shorter; thus boundary scattering becomes less probable unless the thickness of the film is close to the MFP of the phonons responsible for most of the heat transport. For instance, in the case of the 16 nm thick film, the k_r at room temperature decreased by 45% compared to the bulk value, whereas the influence of thickness on its temperature dependence is relatively small. Thus, phonons with MFP > 16 nm contribute substantially to the thermal conductivity with a rather small influence on its temperature dependence.

In conclusion, we investigated the thickness-dependence of the in-plane and cross-plane thermal conductivity of crystalline $SnSe_2$ films. Both show a strong thickness dependence in the range of 16−190 nm, with a 2.5-fold reduction in their values with respect to the bulk values. From this result we directly obtained the thermal conductivity anisotropy ratio, which was found to be independent of the film thickness and approximately 8.4. Importantly, we showed that at high temperatures the in-plane thermal conductivity of suspended $SnSe_2$ films can be reduced by more than ∼50% with respect to the room temperature value. The strong dependence of the thermal conductivity on temperature becomes gradually weaker with decreasing thickness due to the dominant role of phonon boundary scattering. Finally, by using the MFP reconstruction method, we showed that at room temperature the main heat-carrying phonons that contribute to in-plane and cross-plane thermal conductivity have mean free paths of several tens of nanometers.

Our results provide valuable information to understand thermal transport in two-dimensional materials and realize functional devices that require highly anisotropic properties, i.e., thermoelectrics, transistors, and optical sensors or operating at high temperatures. Highly anisotropic 2D layered materials like $SnSe_2$ can provide a through-thickness thermal insulation and heat flow propagation mainly in the in-plane direction. This can be advantageous, for example, in heat-sensitive electronic components, such as microchips, where directional heat flow is necessary to prevent hot spots or for cooling circuits.[50,51] Finally, the ability to manipulate heat propagation through either dimensionality confinement or temperature modifications and the quantitative knowledge of the thermal phonon MFPs give important insights for the design of 2D thermoelectric devices with improved heat management.

■ ASSOCIATED CONTENT

Supporting Information

The Supporting Information is available free of charge at https://pubs.acs.org/doi/10.1021/acs.nanolett.1c03018.

Optical images and atomic force microscopy measurements of the exfoliated $SnSe_2$ films; mean free path reconstruction method; FDTR sensitivity analysis; spot size measurements; single-laser Raman thermometry measurements and FEM calculations; power absorption measurements; Raman thermometry calibration; effect of strain, defects, and nonuniform Raman signal on suspended samples (PDF)

■ AUTHOR INFORMATION

Corresponding Author

Alexandros El Sachat − *Catalan Institute of Nanoscience and Nanotechnology (ICN2), CSIC and BIST, Bellaterra 08193 Barcelona, Spain;* orcid.org/0000-0003-3798-9724; Email: alexandros.elsachat@icn2.cat

Authors

Peng Xiao − *Catalan Institute of Nanoscience and Nanotechnology (ICN2), CSIC and BIST, Bellaterra 08193 Barcelona, Spain; Departamento de Física, Universidad Autónoma de Barcelona, Bellaterra 08193 Barcelona, Spain;* orcid.org/0000-0002-4711-2566

Emigdio Chavez-Angel − *Catalan Institute of Nanoscience and Nanotechnology (ICN2), CSIC and BIST, Bellaterra 08193 Barcelona, Spain;* orcid.org/0000-0002-9783-0806

Stefanos Chaitoglou − *National Center for Scientific Research "Demokritos", 15310 Athens, Greece*

Marianna Sledzinska − *Catalan Institute of Nanoscience and Nanotechnology (ICN2), CSIC and BIST, Bellaterra 08193 Barcelona, Spain;* orcid.org/0000-0001-8592-1121

Athanasios Dimoulas − *National Center for Scientific Research "Demokritos", 15310 Athens, Greece;* orcid.org/0000-0003-3199-1356

Clivia M. Sotomayor Torres − *Catalan Institute of Nanoscience and Nanotechnology (ICN2), CSIC and BIST, Bellaterra 08193 Barcelona, Spain; ICREA, 08010 Barcelona, Spain;* orcid.org/0000-0001-9986-2716

Complete contact information is available at: https://pubs.acs.org/10.1021/acs.nanolett.1c03018

Author Contributions

[⊥]P.X and E.C.-A. contributed equally. The work was conceived by A.E.S. and E.C.-A. The sample fabrication was done by P.X. and S.C., and the Raman characterization was performed by P.X. and A.E.S. The AFM and FDTR characterization was carried out by A.E.S. The MFP reconstruction algorithm and TEM analysis were performed by E.C.-A. P.X., E.C.-A., S.C., M.S., A.D., C.M.S.T., and A.E.S. reviewed and edited the manuscript. C.M.S.T. and A.E.S. supervised the work. All authors have read and agreed to the published version of the manuscript. All authors have given approval to the final version of the manuscript. The manuscript was written by A.E.S. and E.C.-A.

Notes

The authors declare no competing financial interest.

■ ACKNOWLEDGMENTS

This work has been supported by the Severo Ochoa program, the Spanish Research Agency (AEI, Grant SEV-2017-0706), and the CERCA Programme/Generalitat de Catalunya. The authors acknowledge support from Spanish MICINN Project

SIP (Grant PGC2018-101743-B-I00) and the EU Project NANOPOLY (Grant GA 289061). S.C. and A.D. acknowledge financial support from the Flag-Era JTC 2017 Project MELODICA. P.X. acknowledges support by a Ph.D. fellowship from the EU Marie Skłodowska-Curie COFUND PREBIST (Grant Agreement 754558).

■ ABBREVIATIONS

AFM, atomic force microcopy; TEM, transmission electron microscopy; FDTR, frequency domain thermoreflectance; MFP, mean free path; 2LRT, two-laser Raman thermometry

■ REFERENCES

(1) Guo, C.; Tian, Z.; Xiao, Y.; Mi, Q.; Xue, J. Field-Effect Transistors of High-Mobility Few-Layer SnSe 2. *Appl. Phys. Lett.* **2016**, *109* (20), 203104.
(2) Schlaf, R.; Lang, O.; Pettenkofer, C.; Jaegermann, W. Band Lineup of Layered Semiconductor Heterointerfaces Prepared by van Der Waals Epitaxy: Charge Transfer Correction Term for the Electron Affinity Rule. *J. Appl. Phys.* **1999**, *85* (5), 2732−2753.
(3) Li, G.; Ding, G.; Gao, G. Thermoelectric Properties of $SnSe_2$ monolayer. *J. Phys.: Condens. Matter* **2017**, *29* (1), 015001.
(4) Xu, P.; Fu, T.; Xin, J.; Liu, Y.; Ying, P.; Zhao, X.; Pan, H.; Zhu, T. Anisotropic Thermoelectric Properties of Layered Compound SnSe2. *Sci. Bull.* **2017**, *62* (24), 1663−1668.
(5) Sun, B.-Z.; Ma, Z.; He, C.; Wu, K. Anisotropic Thermoelectric Properties of Layered Compounds in SnX2 (X = S, Se): A Promising Thermoelectric Material. *Phys. Chem. Chem. Phys.* **2015**, *17* (44), 29844−29853.
(6) Wang, H.; Gao, Y.; Liu, G. Anisotropic Phonon Transport and Lattice Thermal Conductivities in Tin Dichalcogenides SnS2 and SnSe2. *RSC Adv.* **2017**, *7* (14), 8098−8105.
(7) Roy, T.; Tosun, M.; Hettick, M.; Ahn, G. H.; Hu, C.; Javey, A. 2D-2D Tunneling Field-Effect Transistors Using WSe2/SnSe2 Heterostructures. *Appl. Phys. Lett.* **2016**, *108* (8), 083111.
(8) Su, Y.; Ebrish, M. A.; Olson, E. J.; Koester, S. J. SnSe2 Field-Effect Transistors with High Drive Current. *Appl. Phys. Lett.* **2013**, *103* (26), 263104.
(9) Li, M. O.; Esseni, D.; Nahas, J. J.; Jena, D.; Xing, H. G. Two-Dimensional Heterojunction Interlayer Tunneling Field Effect Transistors (Thin-TFETs). *IEEE J. Electron Devices Soc.* **2015**, *3* (3), 200−207.
(10) Chung, K.-M.; Wamwangi, D.; Woda, M.; Wuttig, M.; Bensch, W. Investigation of SnSe, SnSe2, and Sn2Se3 Alloys for Phase Change Memory Applications. *J. Appl. Phys.* **2008**, *103* (8), 083523.
(11) Rai, R. K.; Islam, S.; Roy, A.; Agrawal, G.; Singh, A. K.; Ghosh, A.; N., R. Morphology Controlled Synthesis of Low Bandgap SnSe2 with High Photodetectivity. *Nanoscale* **2019**, *11* (3), 870−877.
(12) Ding, Y.; Xiao, B.; Tang, G.; Hong, J. Transport Properties and High Thermopower of SnSe2: A Full Ab-Initio Investigation. *J. Phys. Chem. C* **2017**, *121* (1), 225−236.
(13) Huang, Y.; Chen, X.; Zhou, D.; Liu, H.; Wang, C.; Du, J.; Ning, L.; Wang, S. Stabilities, Electronic and Optical Properties of SnSe2(1−x)S2x Alloys: A First-Principles Study. *J. Phys. Chem. C* **2016**, *120* (10), 5839−5847.
(14) Saritha, K.; Suryanarayana Reddy, A.; Ramakrishna Reddy, K. T. Investigation on Optical Properties of SnSe2 Thin Films Synthesized by Two − Stage Process. *Mater. Today Proc.* **2017**, *4* (14), 12512−12517.
(15) Martínez-Escobar, D.; Ramachandran, M.; Sánchez-Juárez, A.; Narro Rios, J. S. Optical and Electrical Properties of SnSe2 and SnSe Thin Films Prepared by Spray Pyrolysis. *Thin Solid Films* **2013**, *535*, 390−393.
(16) Evans, B. L.; Hazelwood, R. A. Optical and Electrical Properties of SnSe2. *J. Phys. D: Appl. Phys.* **1969**, *2* (11), 1507−1516.
(17) Bertrand, Y.; Leveque, G.; Raisin, C.; Levy, F. Optical Properties of SnSe2and SnS2. *J. Phys. C: Solid State Phys.* **1979**, *12* (14), 2907−2916.
(18) Zou, B.; Zhou, Y.; Zhang, X.; Zhang, M.; Liu, K.; Gong, M.; Sun, H. Thickness-Dependent Ultralow In-Plane Thermal Conductivity of Chemical Vapor-Deposited SnSe2 Nanofilms: Implications for Thermoelectrics. *ACS Appl. Nano Mater.* **2020**, *3* (10), 10543−10550.
(19) Liu, X.; Li, Z.; Min, L.; Peng, Y.; Xiong, X.; Lu, Y.; Ao, J.-P.; Fang, J.; He, W.; Li, K.; Wu, J.; Mao, W.; Younis, U.; Divakar Botcha, V. Effect of Stress Layer on Thermal Properties of SnSe2 Few Layers. *J. Alloys Compd.* **2019**, *783*, 226−231.
(20) Minnich, A. J. Determining Phonon Mean Free Paths from Observations of Quasiballistic Thermal Transport. *Phys. Rev. Lett.* **2012**, *109* (20), 205901.
(21) Zhang, H.; Chen, X.; Jho, Y.-D.; Minnich, A. J. Temperature-Dependent Mean Free Path Spectra of Thermal Phonons Along the c -Axis of Graphite. *Nano Lett.* **2016**, *16* (3), 1643−1649.
(22) Sanchez-Martinez, M.-Á.; Alzina, F.; Oyarzo, J.; Sotomayor Torres, C.; Chavez-Angel, E. Impact of the Regularization Parameter in the Mean Free Path Reconstruction Method: Nanoscale Heat Transport and Beyond. *Nanomaterials* **2019**, *9* (3), 414.
(23) Castellanos-Gomez, A.; Buscema, M.; Molenaar, R.; Singh, V.; Janssen, L.; van der Zant, H. S. J.; Steele, G. A. Deterministic Transfer of Two-Dimensional Materials by All-Dry Viscoelastic Stamping. *2D Mater.* **2014**, *1* (1), 011002.
(24) Liu, K.; Liu, H.; Wang, J.; Feng, L. Synthesis and Characterization of SnSe2 Hexagonal Nanoflakes. *Mater. Lett.* **2009**, *63* (5), 512−514.
(25) Gonzalez, J. M.; Oleynik, I. I. Layer-Dependent Properties of SnS2 and SnSe2 Two-Dimensional Materials. *Phys. Rev. B: Condens. Matter Mater. Phys.* **2016**, *94* (12), 125443.
(26) Smith, A. J.; Meek, P. E.; Liang, W. Y. Raman Scattering Studies of SnS2and SnSe2. *J. Phys. C: Solid State Phys.* **1977**, *10* (8), 1321−1323.
(27) Reparaz, J. S.; Chavez-Angel, E.; Wagner, M. R.; Graczykowski, B.; Gomis-Bresco, J.; Alzina, F.; Sotomayor Torres, C. M. A Novel Contactless Technique for Thermal Field Mapping and Thermal Conductivity Determination: Two-Laser Raman Thermometry. *Rev. Sci. Instrum.* **2014**, *85* (3), 034901.
(28) El Sachat, A.; Alzina, F.; Sotomayor Torres, C. M.; Chavez-Angel, E. Heat Transport Control and Thermal Characterization of Low-Dimensional Materials: A Review. *Nanomaterials* **2021**, *11* (1), 175.
(29) Graczykowski, B.; El Sachat, A.; Reparaz, J. S.; Sledzinska, M.; Wagner, M. R.; Chavez-Angel, E.; Wu, Y.; Volz, S.; Wu, Y.; Alzina, F.; Sotomayor Torres, C. M. Thermal Conductivity and Air-Mediated Losses in Periodic Porous Silicon Membranes at High Temperatures. *Nat. Commun.* **2017**, *8* (1), 415.
(30) Qin, G.; Qin, Z.; Wang, H.; Hu, M. On the Diversity in the Thermal Transport Properties of Graphene: A First-Principles-Benchmark Study Testing Different Exchange-Correlation Functionals. *Comput. Mater. Sci.* **2018**, *151*, 153−159.
(31) Gu, X.; Wei, Y.; Yin, X.; Li, B.; Yang, R. Colloquium : Phononic Thermal Properties of Two-Dimensional Materials. *Rev. Mod. Phys.* **2018**, *90* (4), 041002.
(32) Sandell, S.; Maire, J.; Chávez-Ángel, E.; Sotomayor Torres, C. M.; Kristiansen, H.; Zhang, Z.; He, J. Enhancement of Thermal Boundary Conductance of Metal−Polymer System. *Nanomaterials* **2020**, *10* (4), 670.
(33) Sandell, S.; Chávez-Ángel, E.; El Sachat, A.; He, J.; Sotomayor Torres, C. M.; Maire, J. Thermoreflectance Techniques and Raman Thermometry for Thermal Property Characterization of Nanostructures. *J. Appl. Phys.* **2020**, *128* (13), 131101.
(34) Schmidt, A. J.; Cheaito, R.; Chiesa, M. A Frequency-Domain Thermoreflectance Method for the Characterization of Thermal Properties. *Rev. Sci. Instrum.* **2009**, *80* (9), 094901.

https://doi.org/10.1021/acs.nanolett.1c03018
Nano Lett. 2021, 21, 9172−9179

(35) Wiedemeier, H.; Pultz, G.; Gaur, U.; Wunderlich, B. Heat Capacity Measurements of SnSe and SnSe2. *Thermochim. Acta* **1981**, *43* (3), 297−303.
(36) Schmidt, A. J.; Chen, X.; Chen, G. Pulse Accumulation, Radial Heat Conduction, and Anisotropic Thermal Conductivity in Pump-Probe Transient Thermoreflectance. *Rev. Sci. Instrum.* **2008**, *79* (11), 114902.
(37) Siemens, M. E.; Li, Q.; Yang, R.; Nelson, K. A.; Anderson, E. H.; Murnane, M. M.; Kapteyn, H. C. Quasi-Ballistic Thermal Transport from Nanoscale Interfaces Observed Using Ultrafast Coherent Soft X-Ray Beams. *Nat. Mater.* **2010**, *9* (1), 26−30.
(38) Subramanyan, H.; Kim, K.; Lu, T.; Zhou, J.; Liu, J. On the Importance of Using Exact Full Phonon Dispersions for Predicting Interfacial Thermal Conductance of Layered Materials Using Diffuse Mismatch Model. *AIP Adv.* **2019**, *9* (11), 115116.
(39) Liu, X.; Zhang, G.; Zhang, Y.-W. Thermal Conduction across the One-Dimensional Interface between a MoS2 Monolayer and Metal Electrode. *Nano Res.* **2016**, *9* (8), 2372−2383.
(40) Sood, A.; Xiong, F.; Chen, S.; Cheaito, R.; Lian, F.; Asheghi, M.; Cui, Y.; Donadio, D.; Goodson, K. E.; Pop, E. Quasi-Ballistic Thermal Transport Across MoS2 Thin Films. *Nano Lett.* **2019**, *19* (4), 2434−2442.
(41) Yang, F.; Dames, C. Mean Free Path Spectra as a Tool to Understand Thermal Conductivity in Bulk and Nanostructures. *Phys. Rev. B: Condens. Matter Mater. Phys.* **2013**, *87* (3), 035437.
(42) Cuffe, J.; Eliason, J. K.; Maznev, A. A.; Collins, K. C.; Johnson, J. A.; Shchepetov, A.; Prunnila, M.; Ahopelto, J.; Sotomayor Torres, C. M.; Chen, G.; Nelson, K. A. Reconstructing Phonon Mean-Free-Path Contributions to Thermal Conductivity Using Nanoscale Membranes. *Phys. Rev. B: Condens. Matter Mater. Phys.* **2015**, *91* (24), 245423.
(43) Chavez-Angel, E.; Zarate, R. A.; Fuentes, S.; Guo, E. J.; Kläui, M.; Jakob, G. Reconstruction of an Effective Magnon Mean Free Path Distribution from Spin Seebeck Measurements in Thin Films. *New J. Phys.* **2017**, *19* (1), 013011.
(44) Rai, A.; Sangwan, V. K.; Gish, J. T.; Hersam, M. C.; Cahill, D. G. Anisotropic Thermal Conductivity of Layered Indium Selenide. *Appl. Phys. Lett.* **2021**, *118* (7), 073101.
(45) Estrada, D.; Li, Z.; Choi, G.-M.; Dunham, S. N.; Serov, A.; Lee, J.; Meng, Y.; Lian, F.; Wang, N. C.; Perez, A.; Haasch, R. T.; Zuo, J.-M.; King, W. P.; Rogers, J. A.; Cahill, D. G.; Pop, E. Thermal Transport in Layer-by-Layer Assembled Polycrystalline Graphene Films. *npj 2D Mater. Appl.* **2019**, *3* (1), 10.
(46) Chávez-Ángel, E.; Reparaz, J. S.; Gomis-Bresco, J.; Wagner, M. R.; Cuffe, J.; Graczykowski, B.; Shchepetov, A.; Jiang, H.; Prunnila, M.; Ahopelto, J.; Alzina, F.; Sotomayor Torres, C. M. Reduction of the Thermal Conductivity in Free-Standing Silicon Nano-Membranes Investigated by Non-Invasive Raman Thermometry. *APL Mater.* **2014**, *2* (1), 012113.
(47) Cho, J.; Goodson, K. E. Cool Electronics. *Nat. Mater.* **2015**, *14* (2), 136−137.
(48) Liu, W.; Asheghi, M. Thermal Conduction in Ultrathin Pure and Doped Single-Crystal Silicon Layers at High Temperatures. *J. Appl. Phys.* **2005**, *98* (12), 123523.
(49) Asheghi, M.; Leung, Y. K.; Wong, S. S.; Goodson, K. E. Phonon-Boundary Scattering in Thin Silicon Layers. *Appl. Phys. Lett.* **1997**, *71* (13), 1798.
(50) Chung, D.; Takizawa, Y. Performance of Isotropic and Anisotropic Heat Spreaders. *J. Electron. Mater.* **2012**, *41* (9), 2580−2587.
(51) Yamaguchi, S.; Tsunekawa, I.; Komatsu, N.; Gao, W.; Shiga, T.; Kodama, T.; Kono, J.; Shiomi, J. One-Directional Thermal Transport in Densely Aligned Single-Wall Carbon Nanotube Films. *Appl. Phys. Lett.* **2019**, *115* (22), 223104.

https://doi.org/10.1021/acs.nanolett.1c03018
Nano Lett. 2021, 21, 9172−9179